JOURNAL OF SOLID STATE CHEMISTRY **124,** 360–365 (1996)
ARTICLE NO. 0250

Relationship between Crystal Structure and Electrical Properties of the Ca-Rich Region in $(La_{1-x}Ca_x)MnO_{2.97}$

Hideki Taguchi

Research Laboratory for Surface Science, Faculty of Science, Okayama University, Okayama 700, Japan

Received January 29, 1996; in revised form April 19, 1996; accepted April 24, 1996

Perovskite-type $(La_{1-x}Ca_x)MnO_{2.97}$ ($0.90 \leq x \leq 1.00$) were synthesized by a standard ceramic technique. $(La_{1-x}Ca_x)MnO_{2.97}$ exhibits the metal–insulator transition in the range $0.90 \leq x \leq 0.98$. With increasing x, the metal–insulator transition temperature (T_t) decreases and $d\rho/dT$ increases. The decrease in both the angles for Mn–O(1 and 2)–Mn and the number of $3d$ electrons with increasing x makes π-bonding weak. ($La_{0.02}Ca_{0.98}$)$MnO_{2.97}$($x = 0.98$) has the peak at ca. 780 K in the ρ–T curve, and this peak is caused by the oxygen deficiency.

INTRODUCTION

$CaMnO_3$ has an orthorhombic perovskite-type structure with $a = 0.5282$ nm, $b = 0.7452$ nm, and $c = 0.5265$ nm, and exhibits weak ferromagnetism with $T_N = 123$ K (1, 2). Taguchi reported that $CaMnO_{3-\delta}$ is an n-type semiconductor and log ρ (ρ is electrical resistivity) vs $T^{-1/4}$ is linear at low temperature (3). The electrical properties of $CaMnO_{3-\delta}$ are explained by the variable range hopping electrons due to Anderson localization (4).

The electrical properties have been reported on the substitution of the Ca^{2+} ion by the rare earth ion (Ln = La, Nd, Gd, Tb, Ho, and Y) in $CaMnO_3$ (5–8). Orthorhombic perovskite-type $(Ln_{1-x}Ca_x)MnO_{3-\delta}$ exhibits the n-type semiconductor at low temperature. $d\rho/dT$ of these manganates changes from negative to positive at high temperature. Differential thermal analysis (DTA) or differential scanning calorimetry (DSC) indicates that the metal–insulator transition occurs without any crystallographic change. From the magnetic measurements of these manganates, the spin state of the Mn^{3+} ion changes from low to high at the metal–insulator transition temperature (5–8).

The metal–insulator transition temperature (T_t) of $(Ln_{1-x}Ca_x)MnO_{3-\delta}$ decreases with decreasing Ln^{3+} ion content (9). At a particular value of the Ln^{3+} ion content, the metal–insulator transition temperature increases with increasing ionic radius of the Ln^{3+} ion. In the metallic region, $d\rho/dT$ is positive and increases with decreasing Ln^{3+} ion content. The increase of $d\rho/dT$ depends on both the decrease in the Mn–O distance and the number of $3d$ electrons that exist in the Mn^{3+} ion with the high-spin state.

It is interesting to examine the relationship between the crystal structure and the electrical properties of the Ca-rich region in $(La_{1-x}Ca_x)MnO_{3-\delta}$. In the present study, $(La_{1-x}Ca_x)MnO_3$ was synthesized in the range $0.90 \leq x \leq 1.00$. From the measurement of the electrical resistivity, the range that $(La_{1-x}Ca_x)MnO_{3-\delta}$ exhibits the metal–insulator transition was determined. Thereafter, the relationship between the cation–anion–cation overlap and the electrical properties was considered to understand the mechanism of the metal–insulator transition in perovskite-type $(La_{1-x}Ca_x)MnO_{3-\delta}$.

EXPERIMENTAL

$(La_{1-x}Ca_x)MnO_{3-\delta}$ ($0.90 \leq x \leq 1.00$) samples were prepared by a standard ceramic technique. Dried La_2O_3, $CaCO_3$, and MnO_2 powders were weighted in the appropriate proportions and milled for a few hours with acetone. After the mixed powders were dried at 373 K, they were calcined at 1173 K for 12 hr in air, then fired at 1573 K for 24 hr under a flow of pure oxygen gas. For measuring the electrical resistivities of the samples, the powders were pressed into pellet form under a pressure of 50 MPa, and the pellet was sintered at 1573 K for 12 hr under the flow of pure oxygen gas. The samples obtained in this manner were annealed at 973 K for 24 hr under the flow of pure oxygen gas.

The oxygen content in each sample was determined by the oxidation–reduction method (10). The phases of the samples were identified by powder X-ray diffraction with monochromatic Cu$K\alpha$ radiation. The structure refinement was carried out by the Rietveld analysis of the powder X-ray diffraction data with the "RIETAN" program written by Izumi (11). Powder X-ray diffraction data were collected by step scanning over an angular range of $20° \leq 2\theta \leq 100°$ in increments of 0.02° (2θ) with monochromatic Cu$K\alpha$ radiation.

0022-4596/96 $18.00

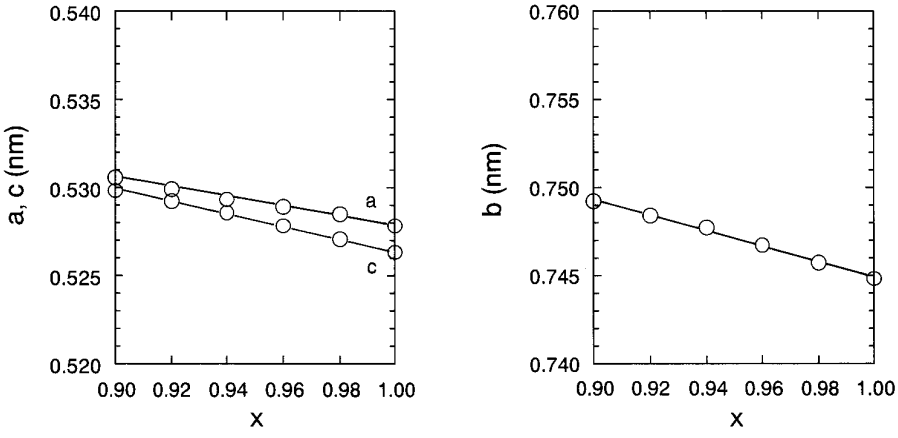

FIG. 1. Cell constants (a, b, and c) vs composition (x) for the system $(La_{1-x}Ca_x)MnO_{2.97}$.

Platinum wires were attached on the sintered samples with platinum paste as electrodes and annealed at 1173 K in air. The electrical resistivity of the samples was measured by a standard four-electrode technique in the temperature range 40–935 K. Differential thermal analysis (DTA) and thermogravimetry (TG) for $(La_{0.02}Ca_{0.98})MnO_{3-\delta}$ (x = 0.98) were performed in the temperature range 300–960 K.

RESULTS AND DISCUSSION

The oxygen content of $(La_{1-x}Ca_x)MnO_{3-\delta}$ ($0.90 \leq x \leq 1.00$) annealed at 973 K for 24 hr under the flow of pure oxygen gas was determined to be ca. 2.97 from chemical analysis. Powder X-ray diffraction patterns of $(La_{1-x}Ca_x)MnO_{2.97}$ ($0.90 \leq x \leq 1.00$) at room temperature were completely indexed as the orthorhombic perovskite-type structure. Figure 1 shows the relationship between the cell constants (a, b, and c axes) and the composition. The cell constants decrease linearly with increasing x. Figure 2 shows the relationship between the cell volume and the composition. The cell volume also decreases linearly with incresing x. The ionic radii of the Ca^{2+} ion and the La^{3+} ion with a coordination number (CN) of 12 are 0.135 and 0.132 nm, respectively (12). Although the ionic radius of the Ca^{2+} ion is larger than that of the La^{3+} ion, both the cell constants and the cell volume decrease with increasing x. The linear decrease in the cell constants and the cell volume is explained by the increase of Mn^{4+} ion content; that is, the ionic radius of the M^{4+} ion is smaller than that of the Mn^{3+} ion located in the octahedral site (12).

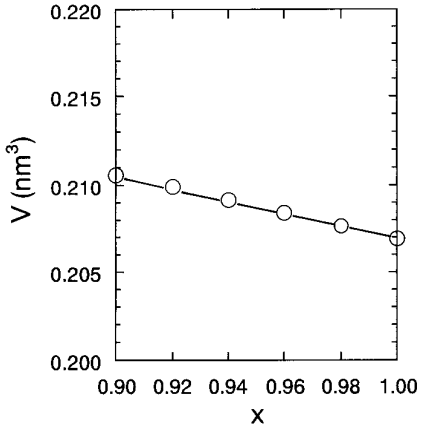

FIG. 2. Cell volume (V) vs composition (x) for the system $(La_{1-x}Ca_x)MnO_{2.97}$.

The structure refinement of $(La_{1-x}Ca_x)MnO_{2.97}$ ($0.90 \leq x \leq 1.00$) was carried out by Rietveld analysis of powder X-ray diffraction data. $(La_{1-x}Ca_x)MnO_{2.97}$ has the orthorhombic $GdFeO_3$-type structure with space group *Pnma* (2). In the present study, isotropic thermal parameters (B) for the La, Ca Mn, O(1), and O(2) ions were fixed at 0.003 nm^2 for all samples. Refined structural parameters and residuals, R_{WP}, R_I, and R_F, are listed in Table 1. R_{WP}, R_I, and R_F are the weighted pattern, the integrated intensity, and the structure factor, respectively. The final R_F of all samples was less than 3.59%, and the low R_F suggests that the structural model for $(La_{1-x}Ca_x)MnO_{2.97}$ is reasonable.

In the orthorhombic $GdFeO_3$-type structure, A-site cations (La and Ca ions) coordinate with 12 anions; 4 O(1) and 8 O(2) ions. B-site cations (Mn ions) coordinate with 6 anions: 2 O(1) and 4 O(2) ions. Table 2 shows the Mn–O distance of $(La_{1-x}Ca_x)MnO_{3-\delta}$ calculated from the refined structure. The Mn–O(1), Mn–O(2) × 2, and Mn–O(2) × 2 distances of $(La_{0.10}Ca_{0.90})MnO_{2.97}$($x$ = 0.90) are 0.191 ± 0.001 nm, 0.187 ± 0.004 nm, and 0.194 ± 0.003 nm, respectively. The Mn–O(1 and 2) distances are independent on the composition. The angles of O–Mn–O and Mn–O–Mn of $(La_{1-x}Ca_x)MnO_{2.97}$ are calculated from the refined structural parameters. The angles for O(1)–Mn–O(1), O(1)–Mn–O(2), and O(2)–Mn–O(2) are 180°, 90°,

TABLE 1
Refined Structure Parameters for $(La_{1-x}Ca_x)MnO_{2.97}$

Atom	Position	x	y	z	B
x = 0.90	a = 0.53063(3) nm		b = 0.74923(5) nm	c = 0.52988(3) nm	
	R_{WP} = 13.85%		R_I = 3.06%	R_F = 3.34%	
La, Ca	4(c)	0.027(1)	0.25	−0.006(3)	0.003
Mn	4(b)	0	0	0.5	0.003
O(1)	4(c)	0.490(4)	0.25	0.067(8)	0.003
O(2)	8(d)	0.280(6)	0.030(4)	−0.289(5)	0.003
x = 0.92	a = 0.52997(3) nm		b = 0.74836(4) nm	c = 0.52931(3) nm	
	R_{WP} = 13.38%		R_I = 3.29%	R_F = 3.13%	
La, Ca	4(c)	0.028(1)	0.25	−0.005(3)	0.003
Mn	4(b)	0	0	0.5	0.003
O(1)	4(c)	0.490(3)	0.25	0.072(8)	0.003
O(2)	8(d)	0.287(4)	0.029(3)	−0.284(5)	0.003
x = 0.94	a = 0.52940(4) nm		b = 0.74770(6) nm	c = 0.52862(4) nm	
	R_{WP} = 14.31%		R_I = 3.61%	R_F = 3.18%	
La, Ca	4(c)	0.029(1)	0.25	−0.006(3)	0.003
Mn	4(b)	0	0	0.5	0.003
O(1)	4(c)	0.488(3)	0.25	0.072(8)	0.003
O(2)	8(d)	0.285(5)	0.030(3)	−0.288(5)	0.003
x = 0.96	a = 0.52896(3) nm		b = 0.74670(5) nm	c = 0.52786(3) nm	
	R_{WP} = 16.08%		R_I = 3.36%	R_F = 3.41%	
La, Ca	4(c)	0.029(1)	0.25	−0.005(4)	0.003
Mn	4(b)	0	0	0.5	0.003
O(1)	4(c)	0.489(4)	0.25	0.074(9)	0.003
O(2)	8(d)	0.281(5)	0.030(4)	−0.292(5)	0.003
x = 0.98	a = 0.52851(2) nm		b = 0.74570(4) nm	c = 0.52711(3) nm	
	R_{WP} = 17.34%		R_I = 3.82%	R_F = 2.89%	
La, Ca	4(c)	0.032(1)	0.25	−0.007(3)	0.003
Mn	4(b)	0	0	0.5	0.003
O(1)	4(c)	0.489(4)	0.25	0.079(8)	0.003
O(2)	8(d)	0.284(4)	0.030(3)	−0.292(4)	0.003
x = 1.00	a = 0.52819(1) nm		b = 0.74547(2) nm	c = 0.52658(1) nm	
	R_{WP} = 13.47%		R_I = 4.74%	R_F = 3.59%	
La, Ca	4(c)	0.034(1)	0.25	−0.005(3)	0.003
Mn	4(b)	0	0	0.5	0.003
O(1)	4(c)	0.491(3)	0.25	0.085(6)	0.003
O(2)	8(d)	0.287(3)	0.030(3)	−0.292(3)	0.003

TABLE 2
Mn–O Distance of $(La_{1-x}Ca_x)MnO_{2.97}$

x	Mn–O(1) (nm)	Mn–(2) × 2 (nm)	Mn–O(2) × 2 (nm)
0.90	0.191(1)	0.187(4)	0.194(3)
0.92	0.191(1)	0.189(3)	0.192(3)
0.94	0.191(1)	0.189(3)	0.192(3)
0.96	0.191(1)	0.186(4)	0.194(3)
0.98	0.191(1)	0.187(3)	0.193(3)
1.00	0.192(1)	0.188(2)	0.192(2)

TABLE 3
Mn–O–Mn Angle (°) for $(La_{1-x}Ca_x)MnO_{2.97}$

x	Mn–O(1)–Mn	Mn–O(2)–Mn
0.90	158.3(25)	159.2(14)
0.92	156.8(24)	159.2(14)
0.94	156.5(26)	158.6(11)
0.96	156.1(29)	158.8(14)
0.98	154.5(24)	158.0(12)
1.00	152.9(18)	157.5(09)

and 90° or 180°, respectively. Table 3 shows the angles for Mn–O(1 and 2)–Mn calculated from the refined structure. The angles for Mn–O(1 and 2)–Mn are less than 180°, and decrease with increasing x. The rate of decrease in the angle for Mn–O(1)–Mn is larger than that in the angle for Mn–O(2)–Mn.

Figure 3 shows the relationship between the logarithm of the electrical resistivity (log ρ) of $(La_{1-x}Ca_x)MnO_{2.97}$ (x = 0.96, 98, and 1.00) and the reciprocal temperature ($1000/T$). At low temperature, all samples are n-type semiconductors, and log ρ increases with increasing x. The energy gap (E_g) calculated from the linear portion of the log ρ–$1000/T$ curves is shown in Fig. 4. E_g is ca. 0.03–0.05 eV in the range $0.90 \leq x \leq 0.98$, and increases abruptly to ca. 0.13 eV for x = 1.00. The temperature dependence of the electrical resistivity indicates that the sample (x = 1.00) is the n-type semiconductor below 953 K, and the log ρ–$1000/T$ curve has a deflection point at ca. 770 K. This point is shown as an arrow in Fig. 3. On the other hand, the log ρ–$1000/T$ curves of the samples ($0.90 \leq x \leq 0.98$) have minimum values. These results indicate that $(La_{1-x}Ca_x)MnO_{2.97}$ exhibits the metal–insulator transition in the range $0.90 \leq x \leq 0.98$. The log ρ–$1000/T$ curves are nonlinear at low temperature, and the log ρ–$T^{-1/4}$ curves are

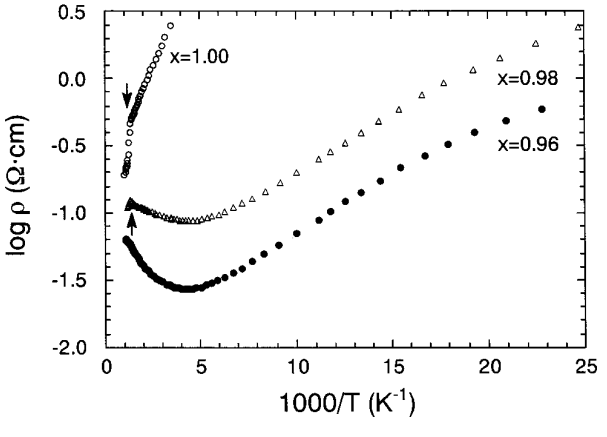

FIG. 3. Logarithm of the electrical resistivity (log ρ) vs $1000/T$ for the system $(La_{1-x}Ca_x)MnO_{2.97}$.

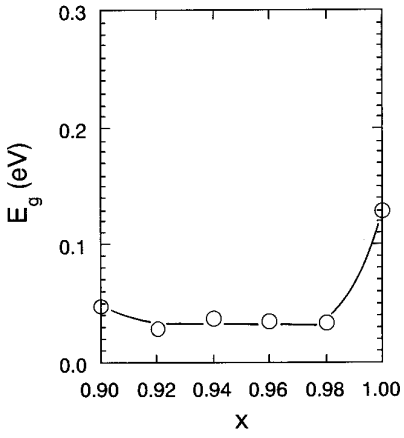

FIG. 4. Energy gap (E_g) vs composition (x) for the system $(La_{1-x}Ca_x)MnO_{2.97}$.

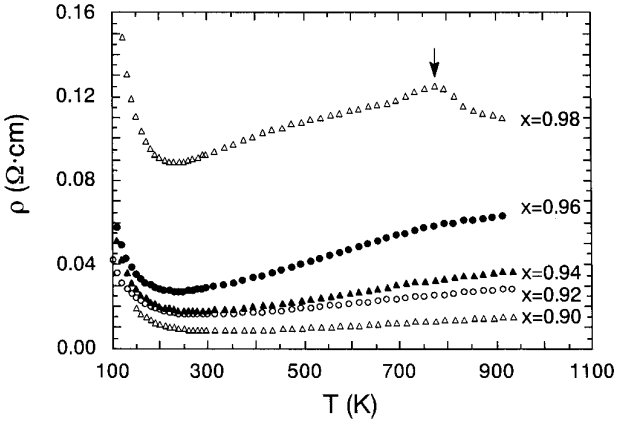

FIG. 6. Electrical resistivity (ρ) vs temperature (T) for the system $(La_{1-x}Ca_x)MnO_{2.97}$.

plotted in Fig. 5. The linear relationship between log ρ and $T^{-1/4}$ indicates that the electrical properties of $(La_{1-x}Ca_x)MnO_{2.97}$ can be related to the variable range hopping of electrons due to Anderson localization (4), which was also reported for other perovskite-type oxides such as $CaMnO_{3-\delta}$(3) and $(Eu_{1-x}Sr_x)FeO_3$ (13).

The relationship between the electrical resistivity (ρ) of $(La_{1-x}Ca_x)MnO_{2.97}$ ($0.90 \le x \le 0.98$) and temperature (T) in the temperature range 100–935 K is shown in Fig. 6. $d\rho/dT$ of the electrical resistivity (ρ) changes from negative to positive with increasing temperature. The electrical resistivity (ρ) of $(La_{0.02}Ca_{0.98})MnO_{2.97}$ ($x = 0.98$) has a peak at ca. 780 K. Taguchi and Shimada reported that the metal–insulator transition of $(La_{1-x}Ca_x)MnO_{3-\delta}$ is caused by the change of the spin state of the Mn^{3+} ion (5). The metal–insulator transition temperature (T_t) is defined as the temperature where $d\rho/dT$ changes from negative to positive. Figure 7 shows the relationship between T_t and the composition. T_t for $x = 0.90$ is ca. 313 K, and decreases monotonically to ca. 229 K ($x = 0.98$). The electrical resistivity (ρ) is generally given by

$$\rho = \rho_o + \rho'\alpha T,$$

where ρ_o is a constant depended on the impurity content, ρ' is a constant, α is a temperature coefficient, and T is temperature (14). As the sintered samples were used to measure the electrical resistivity, we used $d\rho/dT$ which is given by

$$d\rho/dT = \rho'\alpha$$

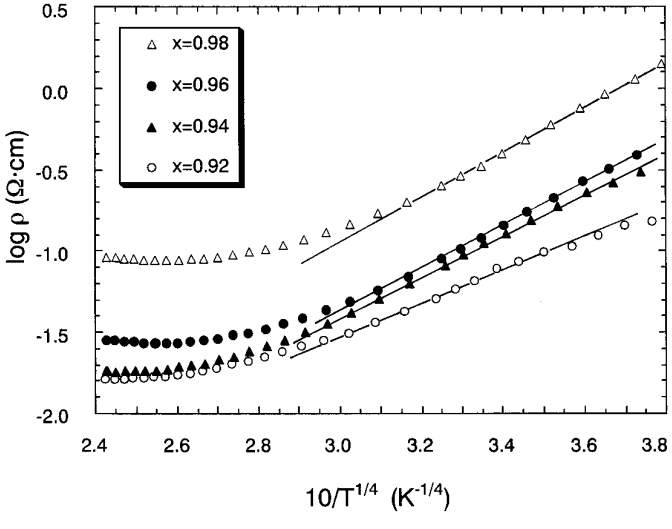

FIG. 5. Logarithm of the electrical resistivity (log ρ) vs $10/T^{1/4}$ for the system $(La_{1-x}Ca_x)MnO_{2.97}$.

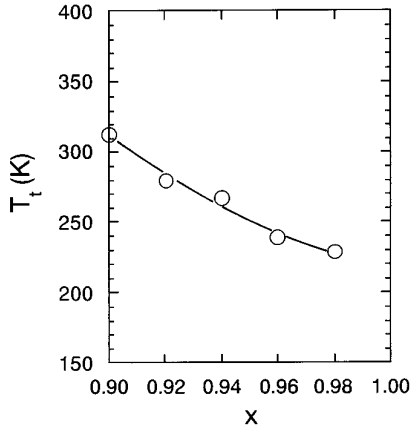

FIG. 7. Metal–insulator transition temperature (T_t) vs composition (x) for the system $(La_{1-x}Ca_x)MnO_{2.97}$.

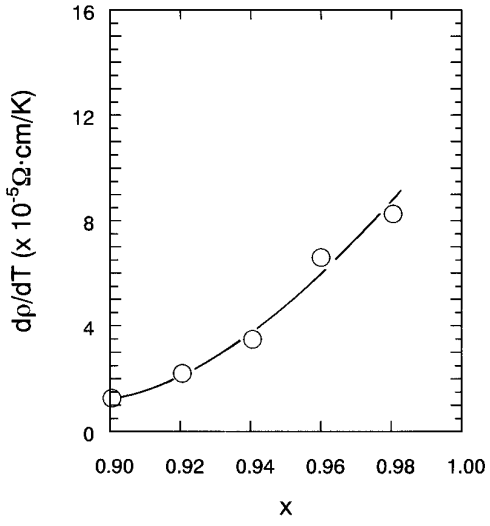

FIG. 8. $d\rho/dT$ vs composition (x) for the system $(La_{1-x}Ca_x)MnO_{2.97}$.

because it is difficult to measure ρ' and α independently. $d\rho/dT$ for $x = 0.90$ is ca. $1.3 \times 10^{-5}\ \Omega \cdot$ cm/K, and increases with increasing x. The relationship between $d\rho/dT$ and the composition is shown in Fig. 8.

From the results of Fig. 6, it is obvious that $(La_{0.02}Ca_{0.98})MnO_{2.97}(x = 0.98)$ exhibits the metal–insulator transition at ca. 240 K, and has the peak at ca. 780 K. DTA and TG measurements were carried out to make clear the appearance of the peak. Figure 9 shows the results of DTA and TG of $(La_{0.02}Ca_{0.98})MnO_{2.97}(x = 0.98)$. The sample gives neither an exothermic nor endothermic peak up to 960 K. The gradual weight loss was observed, and the weight loss at 960 K was ca. 0.17%. These results indicate that the crystal structure of $(La_{0.02}Ca_{0.98})MnO_{2.97}$ did not change below 960 K, and the weight loss was caused by the oxygen deficiency. Taguchi reported the relationship

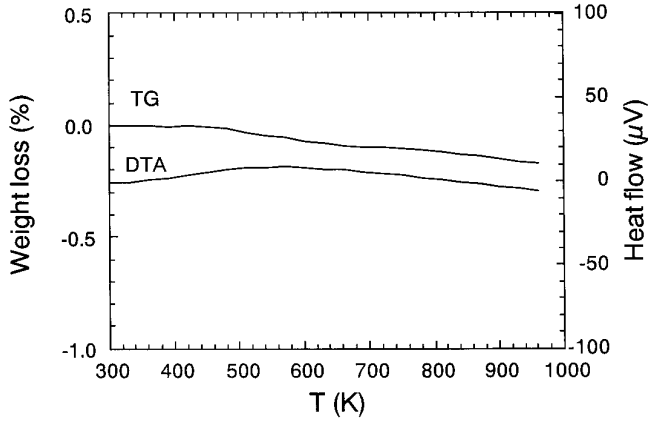

FIG. 9. DTA and TG curves for the system $(La_{0.02}Ca_{0.98})MnO_{2.97}$ ($x = 0.98$).

between the electrical resistivity (ρ) of $CaMnO_{3-\delta}$ and the oxygen content (3). The electrical resistivity (ρ) of $CaMnO_{3-\delta}$ decreases with increasing oxygen deficiency (δ). In the present study, the results of DTA and TG of $(La_{0.02}Ca_{0.98})MnO_{2.97}$ indicate that the oxygen deficiency increases with increasing temperature, so that the electrical resistivity (ρ) decreases and has the peak at ca. 780 K.

The MnO_6 octahedron in $(La_{1-x}Ca_x)MnO_{2.97}$ connects with O(1) or O(2) of the other MnO_6 octahedron. The Mn^{4+} ion has the electron configuration $(d\varepsilon)^3(d\gamma)^0$, and the Mn^{3+} ion has the electron configuration $(d\varepsilon)^4(d\gamma)^0$ or $(d\varepsilon)^3(d\gamma)^1$. There are two kinds of the cation–anion–cation overlap; one is an overlap (π-bonding) between the cation $d\varepsilon$ and oxygen p_π orbitals, and the other is the overlap (σ-bonding) between the cation $d\gamma$ and oxygen p_σ orbitals. Since the Mn–O(1 and 2) distances are independent of the composition as seen in Table 2, it is obvious that the overlap between the cation $d\varepsilon$ and oxygen p_π orbitals decreases with angles for Mn–O(1 and 2)–Mn deviating from 180°. The decrease in both the angles for Mn–O(1 and 2)–Mn and the number of $3d$ electrons with increasing x make π-bonding weak (15), and make 10Dq increase. Therefore, it is observed that log ρ increases the T_t decreases with increasing x.

The mechanism of the metal–insulator transition for $(La_{1-x}Ca_x)MnO_3$ is explained by using the model proposed by Goodenough (16, 17). The band scheme consists of the valence band (localized π^* orbital) and the conduction band (collective σ^* orbital) which are split by the electrostatic field (Δ). The localized π^* orbitals of α and β spins at a given cation are split by the intra-atomic exchange (E_{ex}), and collective σ^* orbitals are likewise split by E_{ex}. The $3d$ electrons in $(La_{1-x}Ca_x)MnO_{2.97}$ exist in the localized π^*-α orbital at low temperature. At high temperature, the spin state of the Mn^{3+} ion changes from low to high. The $3d$ electrons coexist in the localized π^*-α orbital and the localized π^*-β orbital. In the case of $\Delta \leq E_{ex}$, the $3d$ electrons partially filled both the localized π^* orbitals and the collective σ^* orbitals, and $(La_{1-x}Ca_x)MnO_{2.97}$ exhibits metallic behavior. The number of $3d$ electrons in $(La_{1-x}Ca_x)MnO_{2.97}$ is 3.10 for $x = 0.90$, 3.08 for $x = 0.92$, 3.06 for $x = 0.94$, 3.04 for $x = 0.96$, and 3.02 for $x = 0.98$, respectively. Three $3d$ electrons exist in the localized π^* orbital, and the number of $3d$ electrons in the collective σ^* orbitals decreases linearly from 0.10 ($x = 0.90$) to 0.02 ($x = 0.98$). Therefore, as seen in Fig. 8, $d\rho/dT$ increases linearly with decreasing $3d$ electrons in the collective σ^* orbitals.

CONCLUSION

$(La_{1-x}Ca_x)MnO_{2.97}$ exhibits the metal–insulator transition in the range $0.90 \leq x \leq 0.98$. The Mn–O(1 and 2) distances are independent of the composition, while the

angles for Mn–O(1 and 2)–Mn deviate from 180°. The decrease in both the angles for Mn–O(1 and 2)–Mn and the number of 3*d* electrons with increasing *x* makes π-bonding weak. The metal–insulator transition temperature (T_t) decreases with increasing *x*. $d\rho/dT$ in the metallic region increases with decreasing 3*d* electrons in the collective σ^* orbitals.

ACKNOWLEDGMENT

The present work was supported by Grant-in-Aid for Scientific Research 06453078 from the Ministry of Education, Science, and Culture of Japan.

REFERENCES

1. J. B. MacCesney, H. J. Williams, J. F. Potter, and R. C. Sherwood, *Phys. Rev.* **164,** 779 (1967).
2. K. R. Poeppelmeier, M. E. Leonowicz, J. C. Scanlon, and W. B. Yelon, *J. Solid State Chem.* **45,** 71 (1982).
3. H. Taguchi, *Phys. Status Solidi, A* **88,** K79 (1985).
4. N. F. Mott, *Adv. Phys.* **21,** 785 (1972).
5. H. Taguchi and M. Shimada, *J. Solid State Chem.* **63,** 290 (1986).
6. H. Taguchi, M. Nagao, and M. Shimada, *J. Solid State Chem.* **76,** 284 (1988).
7. H. Taguchi, M. Nagao, and M. Shimada, *J. Solid State Chem.* **82,** 8 (1989).
8. T. Kobayahi, H. Takizawa, T. Endo, T. Sato, M. Shimada, H. Taguchi, and M. Nagao, *J. Solid State Chem.* **92,** 116 (1991).
9. H. Taguchi, M. Nagao, and M. Shimada, *J. Solid State Chem.* **97,** 476 (1992).
10. B. E. Gushee, L. Katz, and R. Ward, *J. Am. Chem. Soc.* **79,** 5601 (1957).
11. F. Izumi, *Nippon Kesho Gakkaishi* **27,** 23 (1985). [in Japanese]
12. R. D. Shannon and C. T. Prewitt, *Acta Crystallogr. Sect. B* **25,** 925 (1969).
13. V. Joshi, O. Parkash, G. N. Rao, and C. N. R. Rao, *J. Chem. Soc. Faraday Trans.* **2,** 75 (1979).
14. A. J. Dekker, ''Solid State Physics,'' p. 288. Prentice–Hall, New York, 1957.
15. H. Taguchi, *J. Solid State Chem.* **118,** 367 (1995).
16. J. B. Goodenough, *J. Appl. Phys.* **37,** 1415 (1966).
17. J. B. Goodenough, *Czech. J. Phys. B* **17,** 304 (1967).